iScience

CellPress

Article

Charge Regulation of Self-Assembled Tubules by Protonation for Efficiently Selective and Controlled Drug Delivery

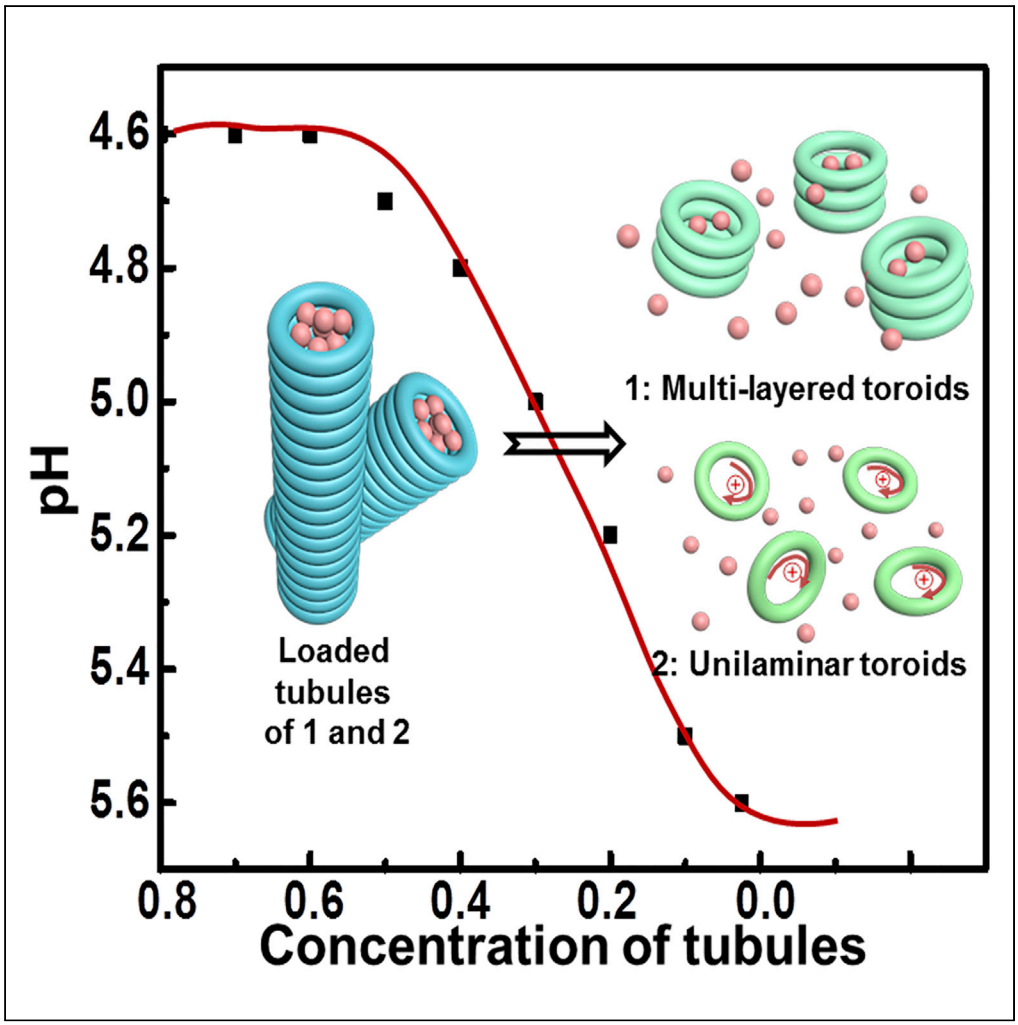

Liping Huang, Hang Zhang, Shanshan Wu, ..., Jianliang Shen, Zong-Wan Mao, Zhegang Huang

shenjl@wibe.ac.cn (J.S.)
cesmzw@mail.sysu.edu.cn (Z.-W.M.)
huangzhg3@mail.sysu.edu.cn (Z.H.)

HIGHLIGHTS

Surface regulation of carriers utilized for drug release

Controlled charge repulsion for efficient drug release

A simple strategy for targeted drug delivery by dynamic assembly

Huang et al., iScience *19*, 224–231
September 27, 2019
https://doi.org/10.1016/j.isci.2019.07.030

iScience

CellPress

Article

Charge Regulation of Self-Assembled Tubules by Protonation for Efficiently Selective and Controlled Drug Delivery

Liping Huang,[1,5] Hang Zhang,[1,5] Shanshan Wu,[1,5] Xin Xu,[1] Lingling Zhang,[1] Hongbing Ji,[1] Liang He,[1] Yuna Qian,[2,3] Zhiyong Wang,[4] Yongming Chen,[4] Jianliang Shen,[2,3,*] Zong-Wan Mao,[1,*] and Zhegang Huang[1,6,*]

SUMMARY

Despite the success for targeted delivery in the body, the efficient release without side effects caused by residual drug remains a challenge. For reducing residual drug, the pH-responsive carriers were prepared by self-assembly from aromatic macrocycles, which were non-toxic and biocompatible. The inner surroundings of aromatic macrocycles could be protonated positively by acid inducing the separation of neighboring macrocycles. Thus, Dox-loaded carriers successfully inhibited the proliferation of carcinoma cells (HepG2 and 4T1) rather than normal cells (HL7702). The effects were further proved *in vivo* without systemic cytotoxicity. Notably, the responsive environment for drug release depended on the concentration of carriers. Particularly, drug release was promoted by carrier separation. Carrier 2 exhibited preferable anticancer efficacy than carrier 1 due to the efficient release of Dox by full separation of the carrier. Collectively, we have developed a novel strategy serving as a selective and controlled drug release platform for cancer therapeutics.

INTRODUCTION

Over the past decades, nanoparticle-based drug delivery systems (NDDs) including liposomes (Mo et al., 2012; Lee et al., 2007; Linderoth et al., 2009), polymeric nanoparticles (Wang et al., 2015; Griset et al., 2009; Tong and Cheng, 2008), and metal-organic frameworks (Horcajada et al., 2010, 2012; Zheng et al., 2016) have received a great deal of attention in the field of cancer therapies. Despite great advances in successful delivery to targeted sites against side effects over free drugs, the release of drugs from carriers at the targeted tissues still remains a challenge in clinical applications. In general, drug release is achieved through acid-responsive systems in the mild acidic environment of the lysosomes or endosomes or the tumor microenvironment (Bae et al., 2003; Du et al., 2011; Zeng et al., 2017). Among them, the labile systems generally rely on pH-responsive hydrolysis, which is unable to ensure targeting delivery. Nevertheless, the hydrolysis in carriers is mostly too stable to release the anticipated dose, thus leading to reduced therapeutic efficacy. Even worse, most of the carriers with residual drugs could be trapped in the major organs such as the liver, heart, and spleen, which may cause side effects in the course of degradation, metabolism, and excretion (Almeida et al., 2011; Arami et al., 2015; Li and Huang, 2008).

The spontaneous assembly of small molecular modules by non-covalent interactions is a key to creating stimuli-responsive systems. Up to now, various strategies for the construction of rapidly responsive supramolecular carriers have been exploited by external triggers such as pH (Duan et al., 2013), redox potential (Zhao et al., 2014), enzyme (Huang et al., 2015), light (Yesilyurt et al., 2011), and ions (Cao et al., 2014). These systems could control drug release effectively through labile chemical interactions by structural collapse. Recently, scientists have developed intelligent devices into carrier systems to create contractive nanoparticles in tumors (Tong et al., 2013). Although the shrinkage of the particles enhanced tissue penetration and retention, a small amount of residual drugs in particles would generate high toxicity or serious inflammation. Among many self-assembled systems, aromatic building blocks have proved promising scaffolds for constructing dynamic architectures (Kim et al., 2011). For example, 120°-folded aromatic segment grafted by hydrophilic oligoether dendrons can easily aggregate into aromatic macrocycles that spontaneously stack on each other to form porous tubules in response to external environments (Wu et al., 2017). As hinted from the dynamic formation of porous tubules based on macrocycle stacking, here we try to vary the charge of the inner surface of tubular carriers by reassembly in mild acidic environment to enhance the repulsion between neighboring macrocycles for facilitating the release of hydrophobic drugs. The porous tubules

[1]Fine Chemical Industry Research Insitute, Key Laboratory for Polymeric Composite & Functional Materials of Ministry of Education and MOE Key Laboratory of Bioinorganic and Synthetic Chemistry Lab, School of Chemistry, Sun Yat-sen University, Guangzhou 510275, PR China

[2]State Key Laboratory of Ophthalmology, Optometry and Vision Science, School of Ophthalmology and Optometry, School of Biomedical Engineering, Wenzhou Medical University, Wenzhou 325027, PR China

[3]Wenzhou Institute, University of Chinese Academy of Sciences, Wenzhou 325001, PR China

[4]Key Laboratory for Polymeric Composite & Functional Materials of Ministry of Education, School of Materials Science and Engineering, Sun Yat-sen University, Guangzhou 510275, PR China

[5]These authors contributed equally

[6]Lead Contact

*Correspondence: shenjl@wibe.ac.cn (J.S.), cesmzw@mail.sysu.edu.cn (Z.-W.M.), huangzhg3@mail.sysu.edu.cn (Z.H.)

https://doi.org/10.1016/j.isci.2019.07.030

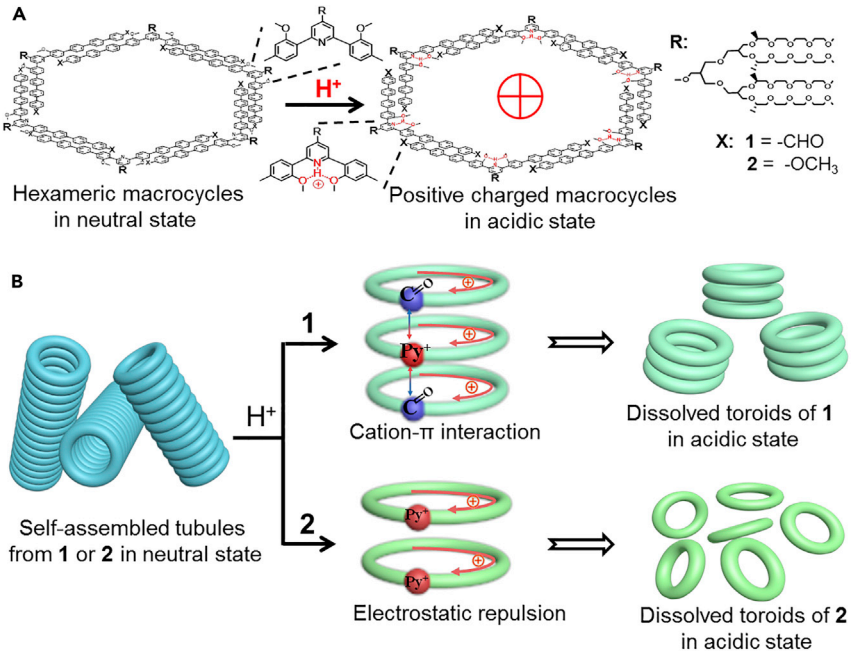

Figure 1. Molecular Structure and Self-Assembly

(A) pH-responsive charge regulation of hexameric macrocycles from self-assembly of bent-shaped aromatic amphiphiles **1** and **2**.

(B) Schematic dissociation of tubular carriers by protonation (multi-layered toroids from self-assembly of **1** based on cation-π interaction. Fully dissociated toroids from self-assembly of **2** by strong electrostatic repulsion).

possess high loading capacity for doxorubicin (Dox) as well as excellent recognition of the proton. Unlike conventional responsive carriers, the tubules dissolve into positively charged macrocycles with hydrophilic cavity. The cationic macrocycles induce a strong electronic repulsion within the inner surroundings of aromatic segment to result in full separation of carriers. Notably, the enhancement of charge in macrocycle leads to preferable expelling ability for drugs (Figure 1).

RESULTS AND DISCUSSION

Molecular Synthesis and Self-Assembly

The responsive tubular deliverers are derived from the self-assembly of bent-shaped aromatic amphiphiles containing a proton-switchable unit of methoxyphenylpyridine-methoxyphenyl triad (ortho-Py) at the inner position, which was decorated with hydrophilic oligoether dendrons at its apex (Figure S1). The bent-shaped aromatic segment with an internal angle of 120° and hydrophilic oligoether dendrons can self-assemble into a hexameric macrocycle owing to its amphiphilic characteristics (Varghese et al., 2005). The aggregation behavior of both molecules in ethanol was studied using vapor pressure osmometry experiments. The molecular weights of **1** and **2** with formyl and methoxyl terminal groups were calculated to be 1,901 and 1,905 Da, respectively. However, in ethanol, the molecular weights of the primary aggregates were measured to be 10,749 and 10,964 Da, respectively (Figure S2), suggesting that both non-covalent macrocycles from **1** and **2** consisted of six molecules. Subsequently, the addition of water into the ethanol solution would drive the hexameric macrocycles to stack on top of each other to form hollow tubules. Transmission electron microscopy (TEM) with negatively stained samples from 0.02 wt. % aqueous solution showed that both molecules self-assembled into elongated objects with an external diameter of 8 nm (Figures 2A, 2C, S3A, and S3B). To further understand the aggregated nanostructures, scanning transmission electron microscopy (STEM) was implemented with a probe aberration corrector. STEM image showed that the 1D objects were separated by dark and white segments, indicative of the formation of hollow tubules with an inner diameter of 3 nm (Figure 2B). The internal and external diameters of the tubules were identical to the fully overlapped hexameric macrocycles, suggesting that the tubules originated from the stacking of macrocyclic hexamer. The highly ordered mesoporosity of the tubules was well suitable as scaffolds for encapsulation of hydrophobic drug in aqueous environment (Figure S4) (Peer et al., 2007; Tian et al., 2014).

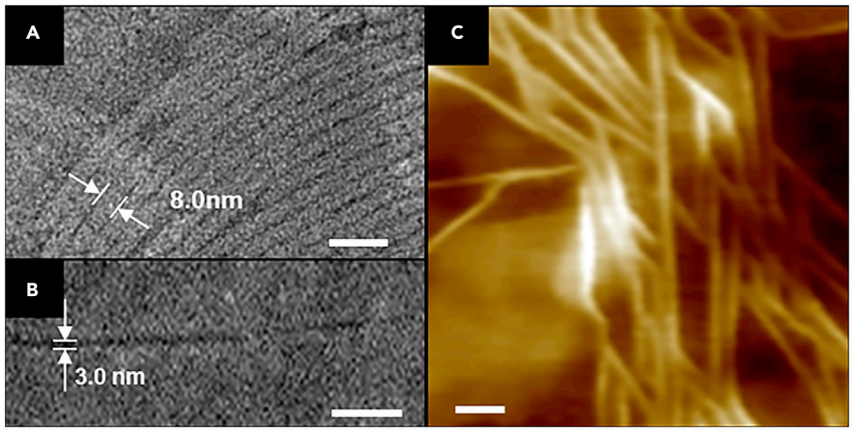

Figure 2. Characterizations of Self-Assembled Tubules

(A) TEM image of negatively stained **2** from 0.02 wt. % aqueous solution; scale bar, 25 nm.

(B) STEM image with a probe aberration corrector of **2** from 0.02 wt. % aqueous solution; scale bar, 25 nm.

(C) AFM image of **2** from 0.02 wt. % aqueous solution with tapping mode; scale bar, 25 nm.

pH-Responsive Properties of Tubular Carriers

We envisioned that the external methoxyl *ortho* to pyridine was responsive to acid, which induced adjacent molecules to slide into a looser packing arrangement due to the stable formation of *ortho*-Py triad through hydrogen bonding. The proton-responsive behavior was confirmed by ^{1}H NMR spectroscopy (Figure 3). Proton nuclear magnetic resonance (^{1}H-NMR) measurements of **2** showed that most protons within *ortho*-Py triad were downfield shifted except the proton *ortho* to pyridine (Ho) by titration of trifluoroacetic acid (TFA), indicating the formation of hydrogen bonds. The Ho proton facing nitrogen atom in the neutral state became shielded by acidification, suggesting a rotation around the C_{Py}-C_{Ph} bond moving away from the NH^{+} group (Leblond et al., 2010). The hydration process allowed the aromatic segments to slide from fully overlapped macrocycles into a looser arrangement to minimize structural crowding at the inner position of aromatic segments. This mechanical sliding of aromatic segments was further confirmed by ultraviolet-visible and fluorescence experiments. Upon addition of TFA, both molecules showed red-shifted absorption and enhanced fluorescence intensity, suggesting that the fully overlapped H-type aggregates changed into slipped J-type aggregates (Figures 4A and S3C) (Wurthner et al., 2011). Remarkably, the expanded macrocycles from J-type aggregation triggered the dissociation of tubules, which reflected in the reduction of hydrodynamic diameter from 168 to 35 nm for **1** and 141 to 26 nm for **2** as confirmed by dynamic light scattering experiments (Figures 4B and S3D). To identify the changed aggregates upon addition of TFA, TEM and atomic force microscopy (AFM) experiments were further performed. TEM images from the stock solutions with 10 equiv. TFA showed toroidal objects with a uniform external diameter of 11 nm and an internal cavity of 4 nm diameter (Figures 4C and 4D), suggesting that the macrocycles were expanded. When the acidic solutions were cast onto mica, both molecules showed discrete toroidal objects. The AFM images of **2** revealed toroidal objects of height 0.3 nm, demonstrating that the toroids are unilaminar macrocycles (Figure 4E). Nevertheless, the toroids of **1** with formyl terminal group showed height close to 3 nm (Figure 4F), suggesting these toroids were formed from multi-layered stacking of macrocycles. The layer-by-layer stacking of charged macrocycles of **1** was attributable to the cation-π interactions of formyl group with neighboring pyridinium nucleus, proved by reduced surface charge from zeta potential measurement (Figure S5) (Yamada et al., 2004). These results demonstrated that the expanded macrocycles could lead the ordered porous objects to dissolve into small aggregates. The kinetic experiment of dynamic assembly revealed that the pH-responsive property depended on the concentration of tubular carriers. In general, lysosomal or endosomal pH in cancer cells (pH 3.8–4.7) shows higher acidity than that in normal cells (pH 4.5–6.0) (Zhang et al., 2016; Kroemer and Jaattela, 2005). Figure S6 showed that when the concentration of carrier was up to 0.6 mg/mL, the structural reorganization can take place mechanically avoiding the release of drugs in the environment of normal cell. Thus the quantity of release could be monitored with 0.6 mg/mL aqueous solution in acidic buffer state (pH 4.6). The released quantity at acidic state was shown in Figure S7, demonstrating that most of the drugs were released from the carriers. Importantly, the difference

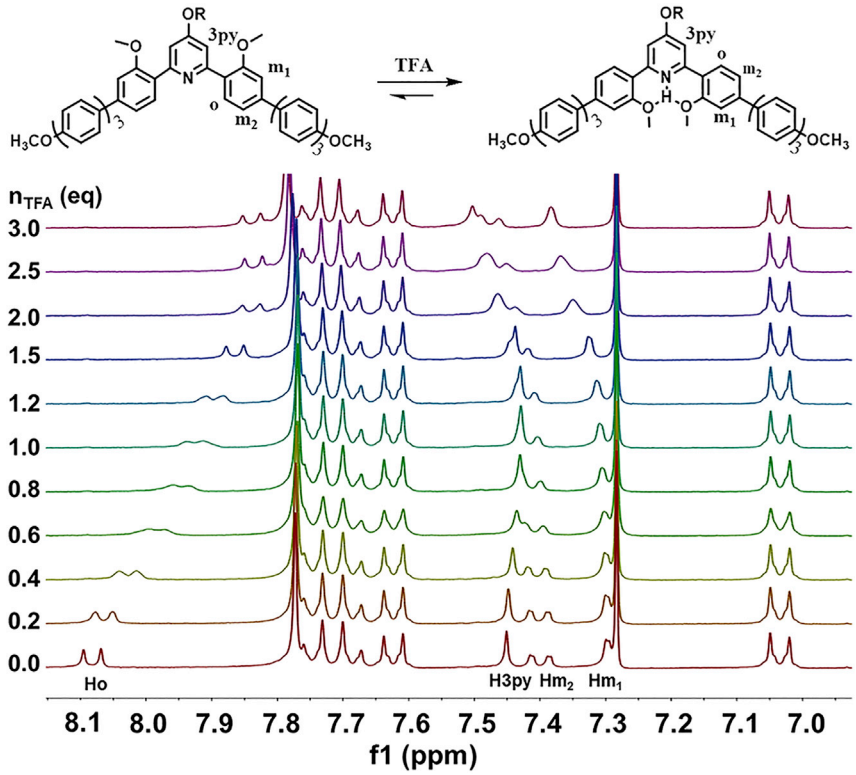

Figure 3. pH-responsive Properties of Aromatic Segment

Representation of transformation of aromatic segment and ^{1}H NMR spectra of **2** (8.4 mM) upon addition of trifluoroacetic acid (TFA).

appeared on the release profile of drugs. The carrier **1** dissolving into multi-layered toroids showed 82%, whereas carrier **2** separating into unilaminar toroids showed up to 95% for the enhanced charge repulsion between NH^+ and cationic Dox.

Evaluation of Carriers *In Vitro* and *In Vivo*

The spontaneous release of drugs in mild acidic state holds great promise for successfully delivering drugs to cancer cells and reducing side effects for normal cells simultaneously. Thus human hepatoma carcinoma cells (HepG2), 4T1 mammary carcinoma cells (4T1), and normal cells (HL7702) were employed as the model to evaluate the *in vitro* cytotoxicity of carriers using the Cell Counting Kit-8 assay. Cell viabilities of HL7702, HepG2, and 4T1 cells co-incubated with carriers **1** and **2** showed above 90% after 72 h (Figures 5A and S8), which meant that both carriers were biocompatible as drug carriers. After loading Dox, both loaded carriers **1** and **2** exhibited higher inhibition of HepG2 and 4T1 cell proliferation but less cytotoxicity to normal cells (HL7702) with the same treatment (Figures 5B and S9–S11). The selective cytotoxicity to HepG2 against HL7702 cells could be explained by selective pH-responsive disaggregation of tubular carriers in the acidic lysosomes of HepG2. To understand the selective behavior, intracellular trafficking of the Dox in cancer cell was observed by confocal laser scanning microscopy (CLSM). The images of CLSM showed that Dox was dominantly co-localized in lysosomes within 6 h and then successfully escaped from lysosomes and entered to the nucleus after 24 h (Figures 5C and S12). Notably, the loaded carrier **2** showed enhanced cytotoxicity than **1** against HepG2 cells (Figures 5B, S9 and S10). To understand preferable inhibition, the quantitative amount of Dox uptaken by HepG2 was observed by flow cytometry. As shown in Figure 5D, accumulations of Dox delivered by both carriers **1** and **2** were gradually increased up to 24 h, which sharply differed from the behaviors of free Dox for the controllable and sustainable drug release. Importantly, the loaded carrier **2** exhibited a preferable accumulation than **1** after 24 h. It can be explained by enhanced charge repulsion between NH^+ and the protonated Dox (Figure S5), which was demonstrated by the release profile of drugs (Figure S7).

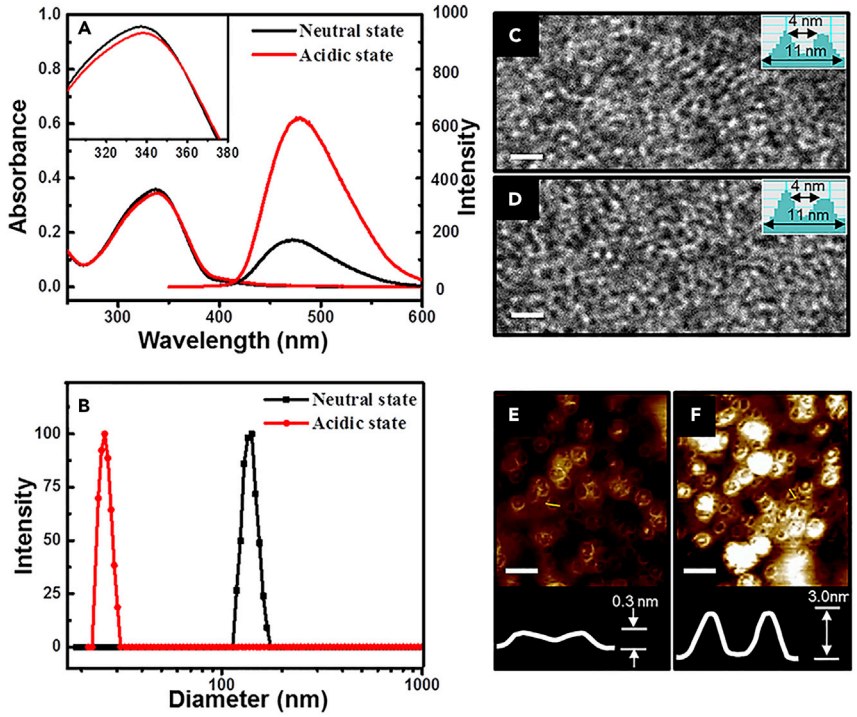

Figure 4. Characterizations of Discrete Toroidal Structures

(A) Absorption (left) and emission (right) of **2** in neutral solution (black line) and CH_3COOH/CH_3COONa buffer solution (red line).

(B) Size distributions of **2** in neutral solution (black line) and CH_3COOH/CH_3COONa buffer solution (red line).

(C and D) TEM images of **1** (C) and **2** (D) from 0.02 wt. % aqueous solution with 10 equiv. TFA; scale bars, 25 nm.

(E and F) AFM images of **1** (E) and **2** (F) from 0.02 wt. % aqueous solution with 10 equiv. TFA; scale bars, 25 nm.

The advances of drug release were also observed *in vivo*. Owing to the enhanced permeability and retention effect, the NDDs preferentially leak into tumor tissues via a permeable tumor vasculature (Davis et al., 2008). Moreover, the carriers surrounded by ethylene oxide chains can hardly be adsorbed by proteins and cleared from the body by the reticuloendothelial system (Knop et al., 2010). To systematically investigate the drug delivery efficiency and the blood retention time of the pH-responsive carriers *in vivo*, the near-infrared (NIR) dye 1,1-dioctadecyl-3,3,3,3-tetramethylindotricarbocyanine iodide (DiR) was encapsulated in carriers **1** and **2**. Then, the carriers labeled by DiR were intravenously injected into 4T1 tumor-bearing nude mice. Subsequently, the real-time imaging of carriers **1** and **2** in the tumor-bearing mice were monitored using *in vivo* imaging system (Figures 5G and S13). The NIR fluorescent signals of DiR-loaded carriers in the tumor tissue gradually increased up to 48 h and maintained the fluorescence until 96 h post-injection. The results indicated that a long retention promoted the tumor accumulation of the tubular carriers. Correspondingly, the antitumor efficiency was evaluated through tumor size changes. As shown in Figures 5E and S14, after 14 days treatment, the groups of Dox-loaded carrier showed higher antitumor efficiency than free Dox and the saline-treated groups. As expected, Dox-loaded carrier **2** exhibited the highest antitumor efficiency for the enhanced drug release, which was confirmed by the intensity of DiR in the tumor site (Figure S15). It was also worth mentioning that no significant difference in body weight was observed during the treatment (Figure 5F). Furthermore, hematoxylin and eosin staining of major organ slices of the treated mice revealed a low systemic toxicity of the tubular carriers (Figures 5H and S16).

Conclusion

We have successfully prepared a kind of pH-responsive drug carrier from the self-assembly of aromatic macrocycles. The aromatic carriers surrounded by ethylene oxide segment exhibited non-toxicity and biocompatibility. The protonation led the macrocycles to be positively charged, which resulted in the separation of porous carriers. Notably, the responsive carriers can recognize external acidic environment fully dependent on the concentration of macrocycles. We found that the carriers dissolved into discrete macrocycles in mild

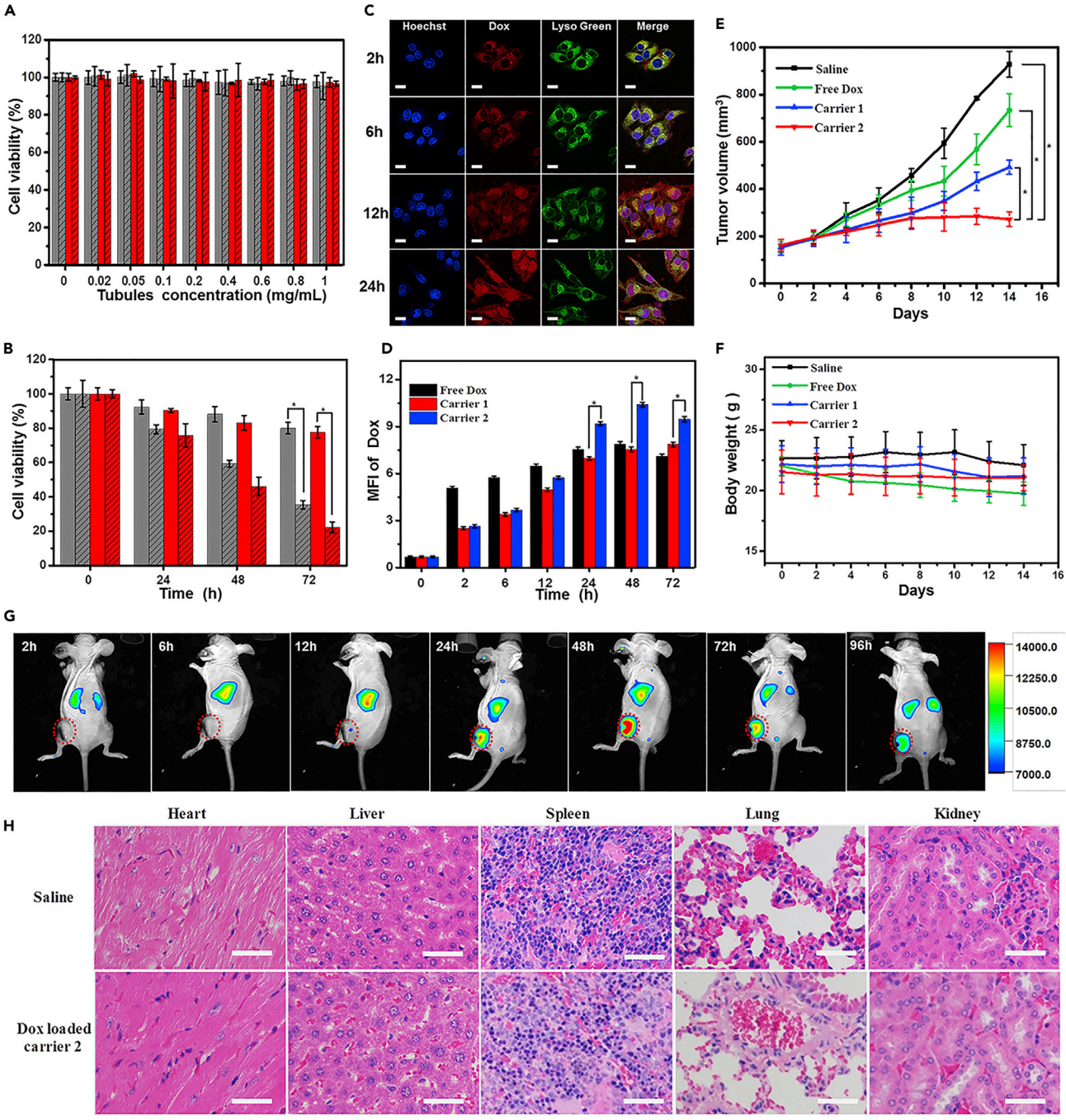

Figure 5. Evaluation of Carriers *In Vitro* and *In Vivo*

(A) Cell Counting Kit-8 assay on cell viability following incubation with carrier **1** for HL7702 (gray without twill) and HepG2 (gray with twill) as well as with carrier **2** for HL7702 (red without twill) and HepG2 (red with twill) for 72 h. Results are presented as mean ± SD (n = 3).

(B) Cell viability of HL7702 (without twill) and HepG2 (with twill) incubated with loaded carrier **1** (gray) as well as loaded carrier **2** (red) by indicated time points. Relative Dox concentration is 0.64 μg/mL; results are presented as mean ± SD (n = 3). *$p < 0.05$.

(C) Intracellular trafficking of Dox-loaded carrier **2** in HepG2 cells. Cells were harvested at the indicated time points (blue, nuclei were stained with Hoechst; red, distribution of Dox; green, lysosomes were labeled by LysoTracker). Scale bars, 20 μm.

(D) Quantitative flow cytometry analysis of Dox-positive HepG2 cancer cells after incubation with indicated groups. Free Dox (black), loaded carrier **1** (red), and loaded carrier **2** (blue). Results are presented as mean ± SD (n = 3). *$p < 0.05$.

Figure 5. *Continued*

(E and F) Mean tumor volumes (E) and body weights (F) of the mice in indicated groups after treatment at different time intervals. Tail intravenous injection into the 4T1 tumor-bearing mice was at a single Dox dose of 3 mg/kg every 2 days. Results are presented as mean ± SD (n = 4). *$p < 0.05$.

(G) *In vivo* real-time imaging of carrier after intravenous injection of DiR-labeled carrier **2** (at a DiR dose of 1 mg/kg).

(H) H&E analyses of the major organs after the last treatment of saline and Dox-loaded carrier **2**; scale bars, 100 μm.

acidic state with the pH close to 4.6. Thus the systems provided efficient anticancer effect with a low systemic cytotoxicity *in vitro* and *in vivo*. In particular, **2** with enhanced positive charge showed preferable inhibition than **1** for the efficient release of drug from the complete separation of carriers. Given these results, the work presented herein provides a practicable strategy for enhanced intracellular drug accumulation by regulating the charge of carriers to prompt efficient release of drug for cancer therapeutics.

Limitations of the Study

Although pH-responsive tubular assembly was successfully used to deliver drugs into cancer cell and reduce the side effect of residual drugs through full dissociation by charge control, responsive carriers lack the specific selectivity for cancer cell. Thus, we will graft a ligand with active targeting into tubular surrounding to develop their special recognition of cancer cell in further study.

METHODS

All methods can be found in the accompanying Transparent Methods supplemental file.

SUPPLEMENTAL INFORMATION

Supplemental Information can be found online at https://doi.org/10.1016/j.isci.2019.07.030.

ACKNOWLEDGMENTS

This work was supported by Sun Yat-sen University, the NSFC (21871299 and 31800833), Guangzhou Science and Technology Program (201707010248), Natural Science Foundation of Guangdong Province (2017A030313086), the Key Laboratory of Functional Inorganic Material Chemistry (Heilongjiang University), Ministry of Education, the Open Project of State Key Laboratory of Supramolecular Structure and Materials (Jilin University), Ministry of Education, and Zhejiang Provincial Natural Science Foundation of China (Z19H180001).

AUTHOR CONTRIBUTIONS

L.H., H.Z., and S.W. contributed equally. L.H. performed most of the experiments and analyzed data. Y.C. and H.J. performed TEM experiment. L.Z. and X.X. performed AFM experiment. H.Z., L.H., Y.Q., J.S., and Z.-W.M. performed *in vitro* and *in vivo* experiments. L.H., S.W., J.S., and Z.H. wrote the paper.

DECLARATION OF INTERESTS

The authors declare no competing interests.

Received: May 13, 2019
Revised: July 16, 2019
Accepted: July 18, 2019
Published: September 27, 2019

REFERENCES

Almeida, J.P.M., Chen, A.L., Foster, A., and Drezek, R. (2011). In vivo biodistribution of nanoparticles. Nanomedicine *6*, 815–835.

Arami, H., Khandhar, A., Liggitt, D., and Krishnan, K.M. (2015). In vivo delivery, pharmacokinetics, biodistribution and toxicity of iron oxide nanoparticles. Chem. Soc. Rev. *44*, 8576–8607.

Bae, Y., Fukushima, S., Harada, A., and Kataoka, K. (2003). Design of environment-sensitive supramolecular assemblies for intracellular drug delivery: polymeric micelles that are responsive to intracellular pH change. Angew. Chem. Int. Ed. *42*, 4640–4643.

Cao, Y., Hu, X.Y., Li, Y., Zou, X.C., Xiong, S.H., Lin, C., Shen, Y.Z., and Wang, L.Y. (2014). Multistimuli-responsive supramolecular vesicles based on water-soluble pillar[6]arene and SAINT complexation for controllable drug release. J. Am. Chem. Soc. *136*, 10762–10769.

Davis, M.E., Chen, Z., and Shin, D.M. (2008). Nanoparticle therapeutics: an emerging treatment modality for cancer. Nat. Rev. Drug Discov. *7*, 771–782.

Du, J.-Z., Du, X.-J., Mao, C.-Q., and Wang, J. (2011). Tailor-made dual pH-sensitive polymer-doxorubicin nanoparticles for efficient anticancer drug delivery. J. Am. Chem. Soc. *13*, 17560–17563.

Duan, Q.P., Cao, Y., Li, Y., Hu, X.Y., Xiao, T.X., Lin, C., Pan, Y., and Wang, L.Y. (2013). pH-responsive supramolecular vesicles based on water-soluble

pillar[6]arene and ferrocene derivative for drug delivery. J. Am. Chem. Soc. *135*, 10542–10549.

Griset, A.P., Walpole, J., Liu, R., Gaffey, A., Colson, Y.L., and Grinstaff, M.W. (2009). Expansile nanoparticles: synthesis, characterization, and in vivo efficacy of an acid-responsive polymeric drug delivery system. J. Am. Chem. Soc. *131*, 2469–2471.

Horcajada, P., Chalati, T., Serre, C., Gillet, B., Sebrie, C., Baati, T., Eubank, J.F., Heurtaux, D., Clayette, P., Kreuz, C., et al. (2010). Porous metal-organic-framework nanoscale carriers as a potential platform for drug delivery and imaging. Nat. Mater. *9*, 172–178.

Horcajada, P., Gref, R., Baati, T., Allan, P.K., Maurin, G., Couvreur, P., Ferey, G., Morris, R.E., and Serre, C. (2012). Metal-organic frameworks in biomedicine. Chem. Rev. *112*, 1232–1268.

Huang, P., Gao, Y., Lin, J., Hu, H., Liao, H.S., Yan, X.F., Tang, Y.X., Jin, A., Song, J.B., Niu, G., et al. (2015). Tumor-specific formation of enzyme-instructed supramolecular self-assemblies as cancer theranostics. ACS Nano *9*, 9517–9527.

Kim, H.-J., Kim, T., and Lee, M. (2011). Responsive nanostructures from aqueous assembly of rigid-flexible block molecules. Acc. Chem. Res. *44*, 72–82.

Knop, K., Hoogenboom, R., Fischer, D., and Schubert, U.S. (2010). Poly(ethylene glycol) in drug delivery: pros and cons as well as potential alternatives. Angew. Chem. Int. Ed. *49*, 6288–6308.

Kroemer, G., and Jaattela, M. (2005). Lysosomes and autophagy in cell death control. Nat. Rev. Cancer *5*, 886–897.

Leblond, J., Gao, H., Petitjean, A., and Leroux, J.C. (2010). pH-responsive molecular tweezers. J. Am. Chem. Soc. *25*, 8544–8545.

Lee, S.M., Chen, H., Dettmer, C.M., O'Halloran, T.V., and Nguyen, S.T. (2007). Polymer-caged liposomes: a pH-Responsive delivery system with high stability. J. Am. Chem. Soc. *129*, 15096–15097.

Li, S.D., and Huang, L. (2008). Pharmacokinetics and biodistribution of nanoparticles. Mol. Pharm. *5*, 496–504.

Linderoth, L., Fristrup, P., Hansen, M., Melander, F., Madsen, R., Andresen, T.L., and Peters, G.H. (2009). Mechanistic study of the sPLA2-mediated hydrolysis of a thio-ester pro anticancer ether lipid. J. Am. Chem. Soc. *131*, 12193–12200.

Mo, R., Sun, Q., Xue, J.W., Li, N., Li, W.Y., Zhang, C., and Ping, Q.N. (2012). Multistage pH-responsive liposomes for mitochondrial-targeted anticancer drug delivery. Adv. Mater. *24*, 3659–3665.

Peer, D., Karp, J.M., Hong, S., Farokhzad, O.C., Margalit, R., and Langer, R. (2007). Nanocarriers as an emerging platform for cancer therapy. Nat. Nanotechnol. *2*, 751–760.

Tian, J., Zhou, T.Y., Zhang, S.C., Aloni, S., Altoe, M.V., Xie, S.H., Wang, H., Zhang, D.W., Zhao, X., Liu, Y., and Li, Z.T. (2014). Three-dimensional periodic supramolecular organic framework ion sponge in water and microcrystals. Nat. Commun. *5*, 5574.

Tong, R., and Cheng, J.J. (2008). Paclitaxel-initiated, controlled polymerization of lactide for the formulation of polymeric nanoparticulate delivery vehicles. Angew. Chem. Int. Ed. *47*, 4830–4834.

Tong, R., Chiang, H.H., and Kohane, D.S. (2013). Photoswitchable nanoparticles for in vivo cancer chemotherapy. Proc. Natl. Acad. Sci. U S A *110*, 19048–19053.

Varghese, R., George, S.J., and Ajayaghosh, A. (2005). Anion induced modulation of self-assembly and optical properties in urea end-capped oligo(p-phenylenevinylene)s. Chem. Commun. 593–595, https://doi.org/10.1039/B413909G.

Wang, D.L., Zhao, T.Y., Zhu, X.Y., Yan, D.Y., and Wang, W.X. (2015). Bioapplications of hyperbranched polymers. Chem. Soc. Rev. *44*, 4023–4071.

Wu, S.S., Li, Y.G., Xie, S.Y., Ma, C., Lim, J., Zhao, J., Kim, D.S., Yang, M., Yoon, D.K., Lee, M., et al. (2017). Supramolecular nanotubules as a catalytic regulator for palladium cations: applications in selective catalysis. Angew. Chem. Int. Ed. *56*, 11511–11514.

Wurthner, F., Kaiser, T.E., and Saha-Moller, C.R. (2011). J-aggregates: from serendipitous discovery to supramolecular engineering of functional dye materials. Angew. Chem. Int. Ed. *50*, 3376–3410.

Yamada, S., Misono, T., and Tsuzuki, S. (2004). Cation-π interactions of a thiocarbonyl group and a carbonyl group with a pyridinium nucleus. J. Am. Chem. Soc. *126*, 9682–9872.

Yesilyurt, V., Ramireddy, R., and Thayumanavan, S. (2011). Photoregulated release of noncovalent guests from dendritic amphiphilic nanocontainers. Angew. Chem. Int. Ed. *50*, 3038–3042.

Zeng, X., Liu, G., Tao, W., Ma, Y., Zhang, X., He, F., Pan, J., Mei, L., and Pan, G. (2017). A drug-self-gated mesoporous antitumor nanoplatform based on pH-sensitive dynamic covalent bond. Adv. Funct. Mater. *27*, 1605985.

Zhang, J.Y., Liu, Z.N., Lian, P., Qian, J., Li, X.W., Wang, L., Fu, W., Chen, L., Wei, X.B., and Li, C. (2016). Selective imaging and cancer cell death via pH switchable near-infrared fluorescence and photothermal effects. Chem. Sci. *7*, 5995–6005.

Zhao, F., Yin, H., and Li, J. (2014). Supramolecular self-assembly forming a multifunctional synergistic system for targeted co-delivery of gene and drug. Biomaterials *35*, 1050–1062.

Zheng, H.Q., Zhang, Y.N., Liu, L.F., Wan, W., Guo, P., Nystrom, A.M., and Zou, X.D. (2016). One-pot synthesis of metal organic frameworks with encapsulated target molecules and their applications for controlled drug delivery. J. Am. Chem. Soc. *138*, 962–968.

ISCI, Volume *19*

Supplemental Information

Charge Regulation of Self-Assembled Tubules by Protonation for Efficiently Selective and Controlled Drug Delivery

Liping Huang, Hang Zhang, Shanshan Wu, Xin Xu, Lingling Zhang, Hongbing Ji, Liang He, Yuna Qian, Zhiyong Wang, Yongming Chen, Jianliang Shen, Zong-Wan Mao, and Zhegang Huang

1. Supplemental Figures.

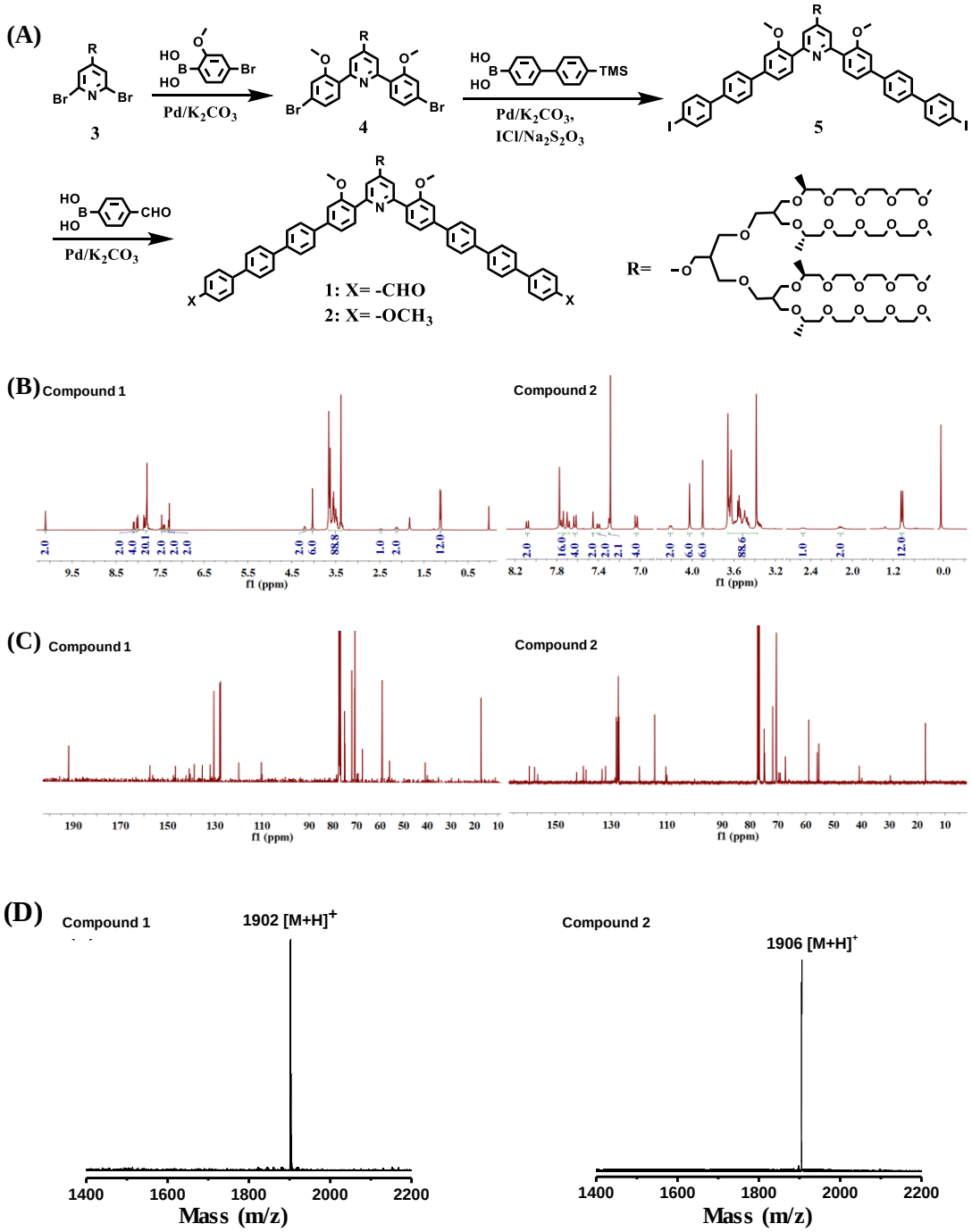

Figure S1. Synthesis scheme and characterizations of molecule 1 and 2. (A). Synthesis scheme of bent-shaped aromatic amphiphiles. ^{1}H-NMR spectra (B), ^{13}C-NMR spectra (C) and MALDI-TOF mass spectra (D) of **1** and **2**. Related to Figure 1.

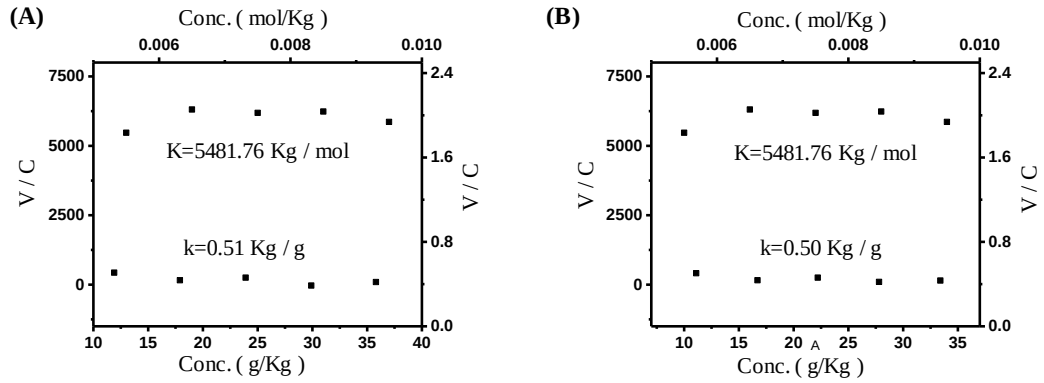

Figure S2. Primary aggregation of hexameric macrocycles. RTs was used as a standard for the determination of K of the instrument, K = 5481.76 Kg/mol. (A) **1** as sample, k = 0.51 Kg/g. Molecular Weight = K/k = 10749 g/mol. Calculated for $(\mathbf{1})_6$: 11406 g/mol. (B) **2** as sample, k = 0.50 Kg/g. Molecular Weight = K/k = 10964 g/mol. Calculated for $(\mathbf{2})_6$: 11430 g/mol. Related to Figure 1.

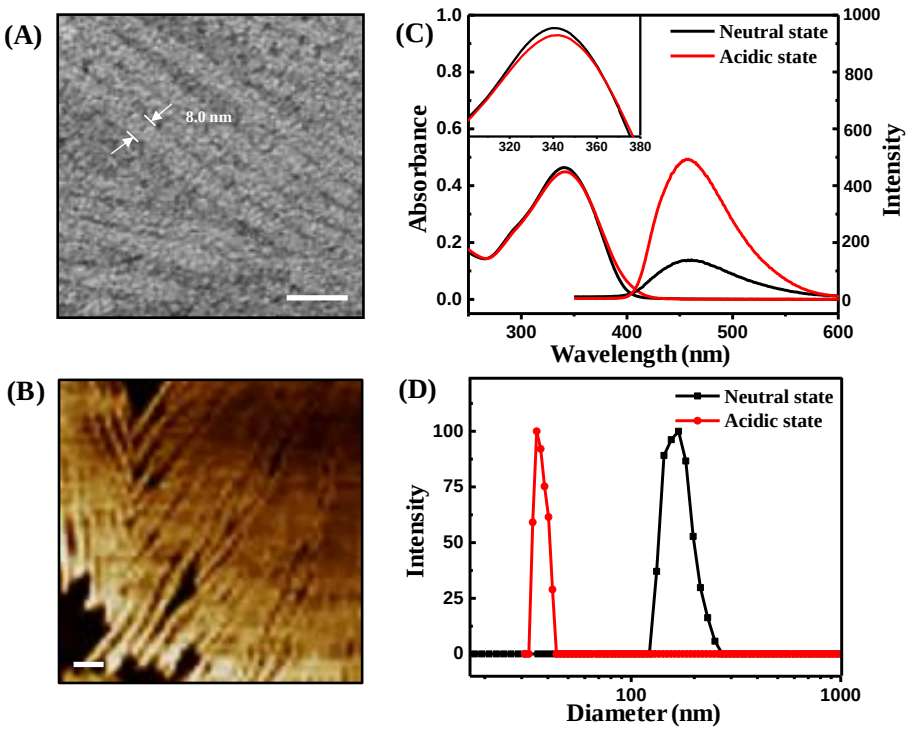

Figure S3. **Characterization of tubular carrier 1.** TEM (A) and AFM (B) images of **1** from 0.02 wt% aqueous solution (both scale bars are 25 nm). (C) Absorption (left) and emission (right) of **1** in neutral solution (black line) and CH_3COOH/CH_3COONa buffer solution at pH 4.6 (red line). (D) Size distributions of **1** in neutral solution (black line) and pH 4.6 buffer solution (red line). Related to Figures 2 and 4.

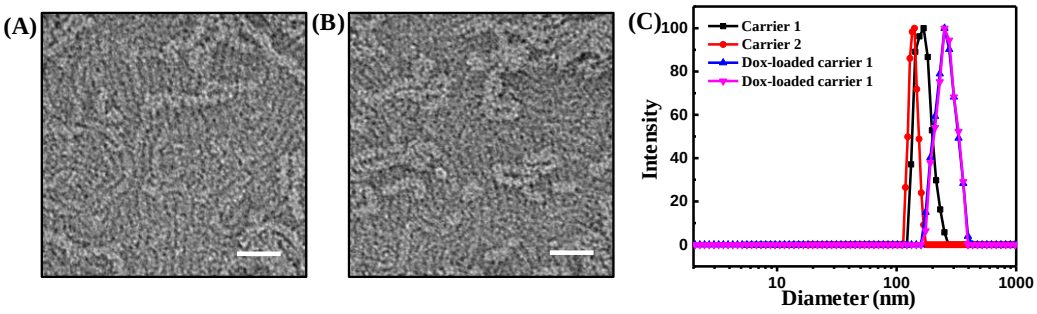

Figure S4. **The carriers with and without drug.** TEM images of Dox-loaded carrier **1** (A) and **2** (B) from 0.02 wt% solution (both scale bars are 50 nm). (C) Size distributions of **1** and **2** with and without Dox from 0.02 wt% solution. Related to Figure 5.

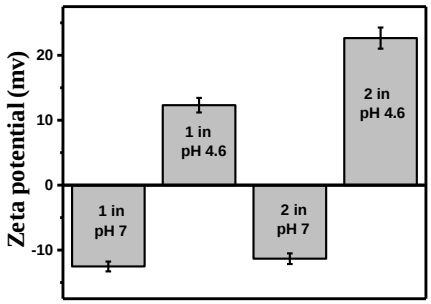

Figure S5. **Surface charge of carrier 1 and 2.** Zeta potential of carrier **1** and **2** in neutral aqueous solution (pH 7) and acidic CH_3COOH/CH_3COONa buffer solution (pH 4.6). Results are presented as mean ± s.d. (n=3). Related to Figures 2 and 4.

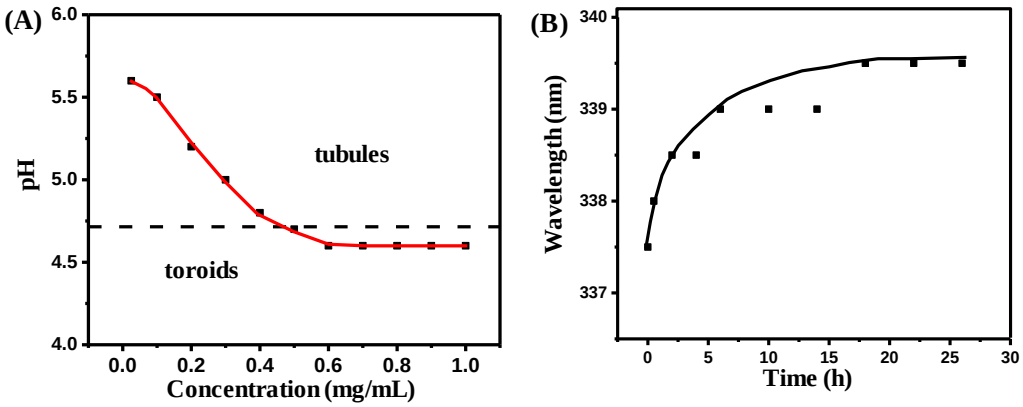

Figure S6. pH-responsive behavior and kinetic response. (A) The curve of structural transformation in terms of the concentration versus to pH value. (Tubular structure: above the red solid line, toroidal structure: below the red solid line). (B) The change of maximum absorption wavelength of **2** (0.6 mg/mL) in the process of dynamic assembly from tubules to toroids against time. Related to Figures 2 and 4.

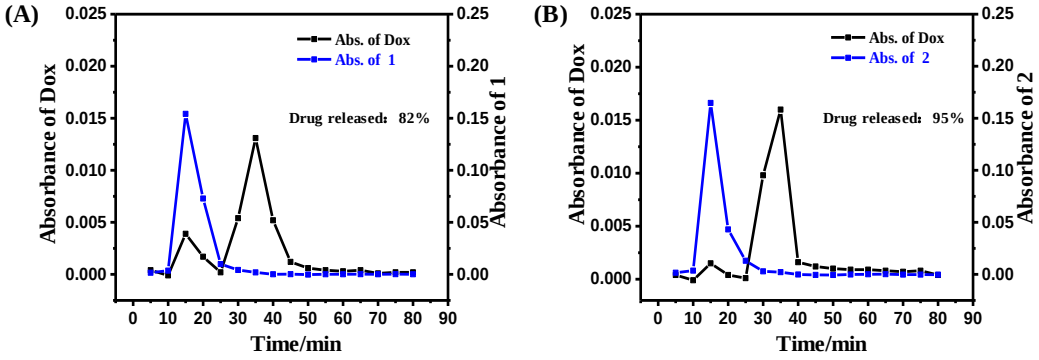

Figure S7. Drug release from carriers. The pH-responsive released Dox from the loaded carrier **1** (A) and **2** (B) using a Sephadex G-50 column after transferring to CH_3COOH/CH_3COONa buffer solutions at pH 4.6 for 24 h by tracing Uv-vis. (Dox: black line; Tubules: blue line). Related to Figure 4.

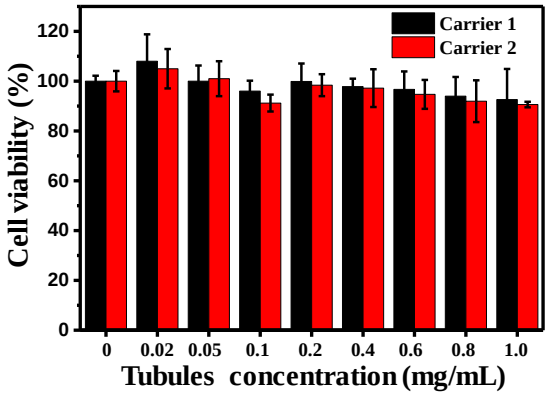

Figure S8. Cytotoxicity of carriers against 4T1 cells. Cell viabilities of 4T1 cells were treated by carrier **1** and **2** at indicated concentrations after incubation for 72 h. Results are presented as mean ± s.d. (n=3). Related to Figure 5.

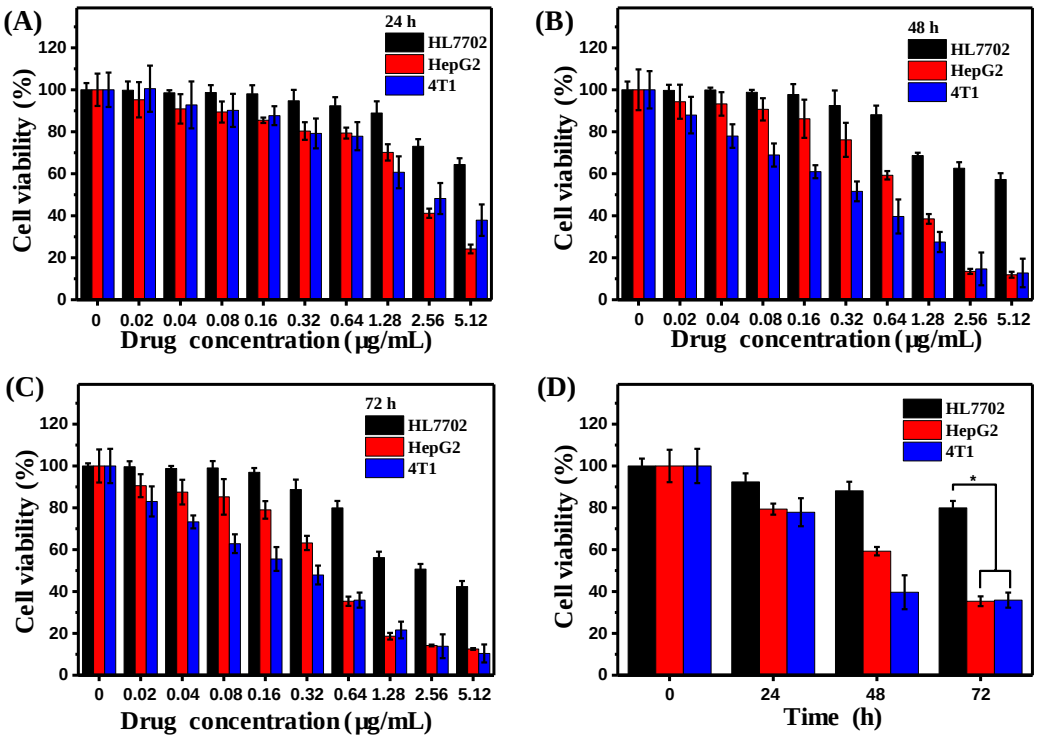

Figure S9. *In vitro* effects of Dox-loaded carrier 1. Cell viabilities of HL7702, HepG2 and 4T1 cells were treated by Dox- loaded carrier **1** at indicated concentrations after incubation for 24 (A), 48 (B) and 72h (C). (D) Cell viabilities of HL7702, HepG2 and 4T1 cells were treated by Dox-loaded carrier **1** at various of time points, and relative concentration of Dox is 0.64 μg/mL. Results are presented as mean ± s.d. (n=3). *, $p<0.05$. Related to Figure 5.

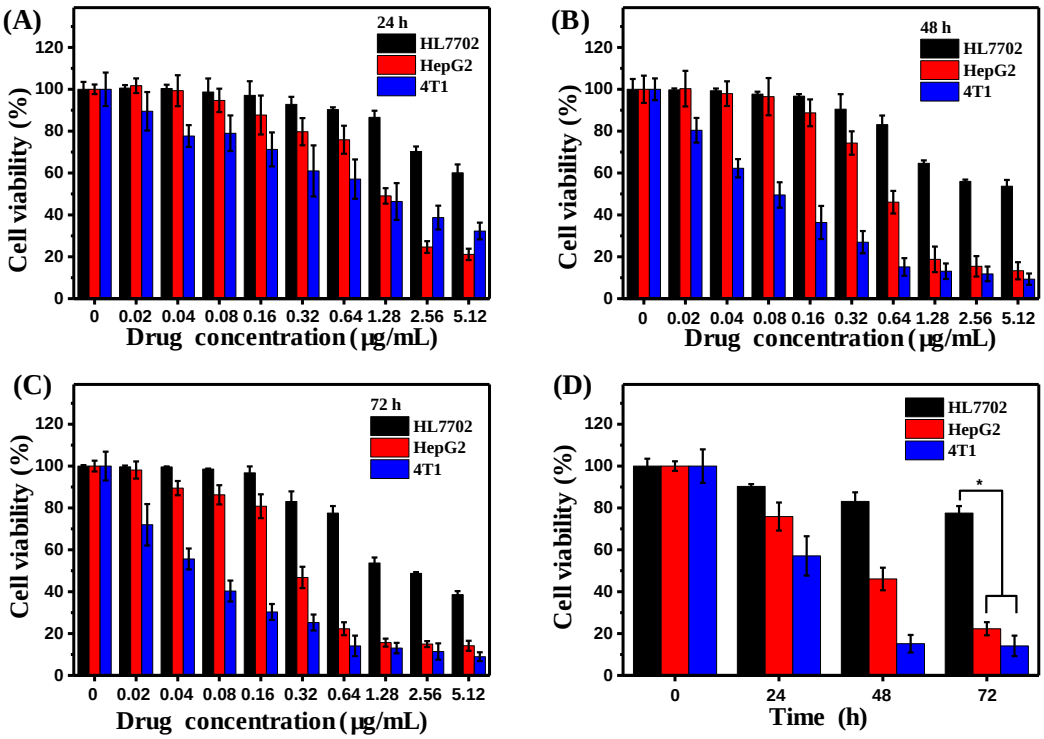

Figure S10. ***In vitro*** **effects of Dox-loaded carrier 2.** Cell viabilities of HL7702, HepG2 and 4T1 cells were treated by Dox-loaded carrier **2** at indicated concentrations after incubation for 24 (A), 48 (B) and 72 h (C). (D) Cell viabilities of HL7702, HepG2 and 4T1 cells was treated by Dox loaded carrier **2** at various of time points, and relative concentration of Dox is 0.64 μg/mL. Results are presented as mean ± s.d. (n=3). *, $p<0.05$. Related to Figure 5.

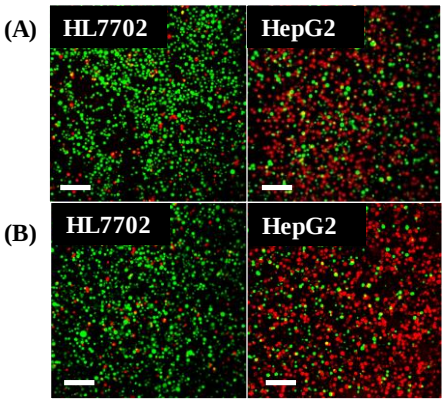

Figure S11. The images of live/dead cells. Cell viabilities staining of HL7702 and HepG2 cells after incubation with Dox-loaded carrier **1** (A) and **2** (B) for 72 h, respectively. Relative Dox concentration is 0.64 μg/mL. Live cells were stained green with Calcein-AM, and dead cells were stained red with PI. All scale bars are 200 μm. Related to Figure 5.

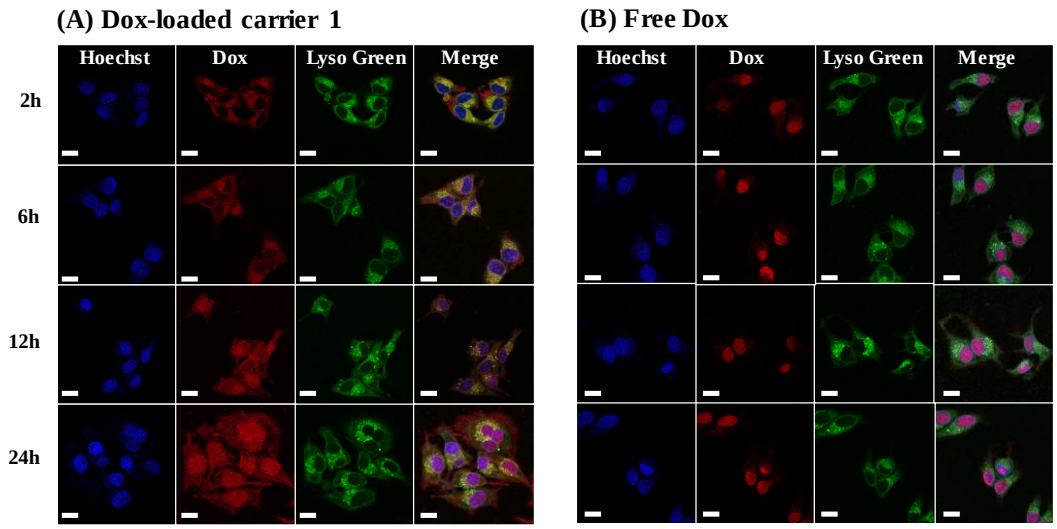

Figure S12. Intracellular trafficking of Dox in HepG2 cells treated by Dox-loaded carrier 1 (A) and free Dox(B). Cells were harvested at the indicated time points (Blue color: Nuclei were stained with Hoechst; Red color: Distribution of Dox; Green color: Lysosomes were labeled by Lysotracker). All scale bars are 20 μm. Related to Figure 5.

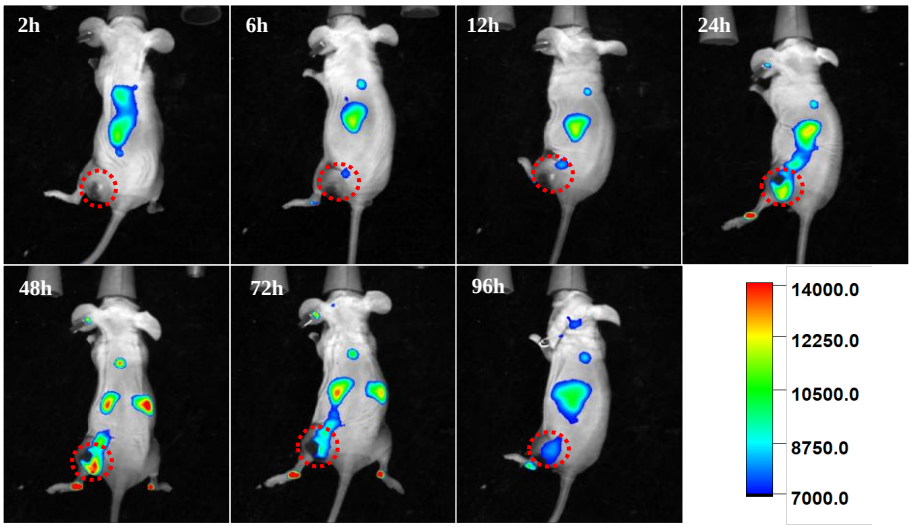

Figure S13. *In vivo* tracing of DiR-labeled carrier 1. *In vivo* real-time imaging of DiR-labeled carrier **1** by intravenous injection after various time points.The red-dashed circle indicated the tumor site of mice. Related to Figure 5.

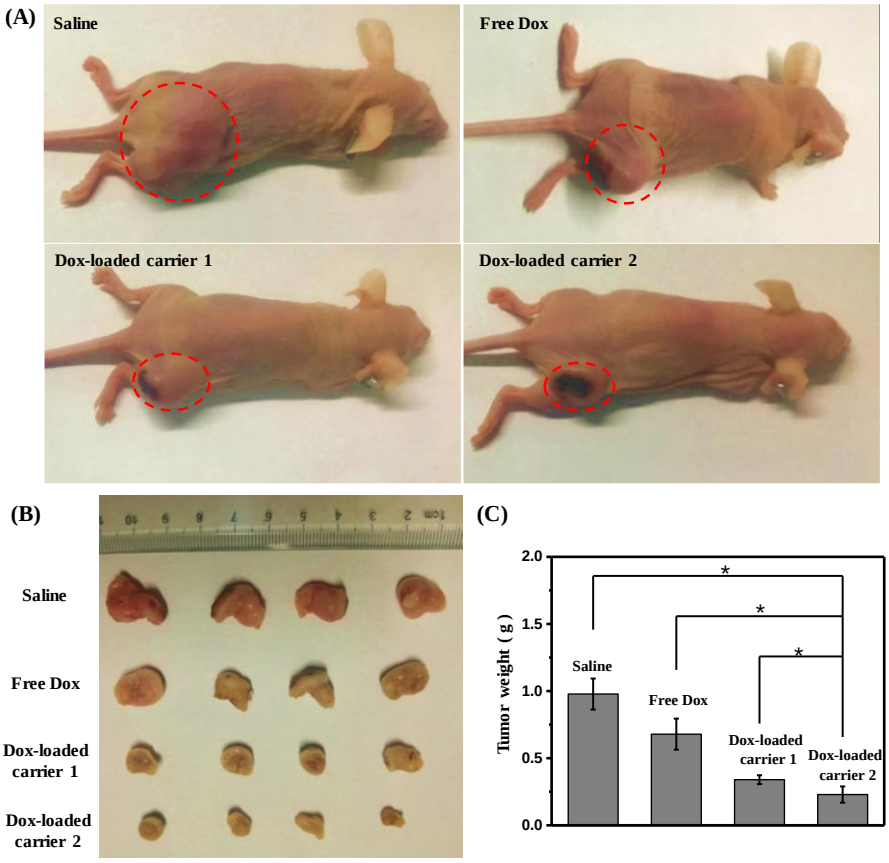

Figure S14. *In vivo* antitumor effects. (A) Representative images of mice bearing 4T1 tumors after 14 d of different treatments. (B) Morphology and (C) mean weights of tumors removed from the sacrificed mice in all groups at the end of point of study. Data are presented as means ± s.d. (n=4), *, p <0.05. Related to Figure 5.

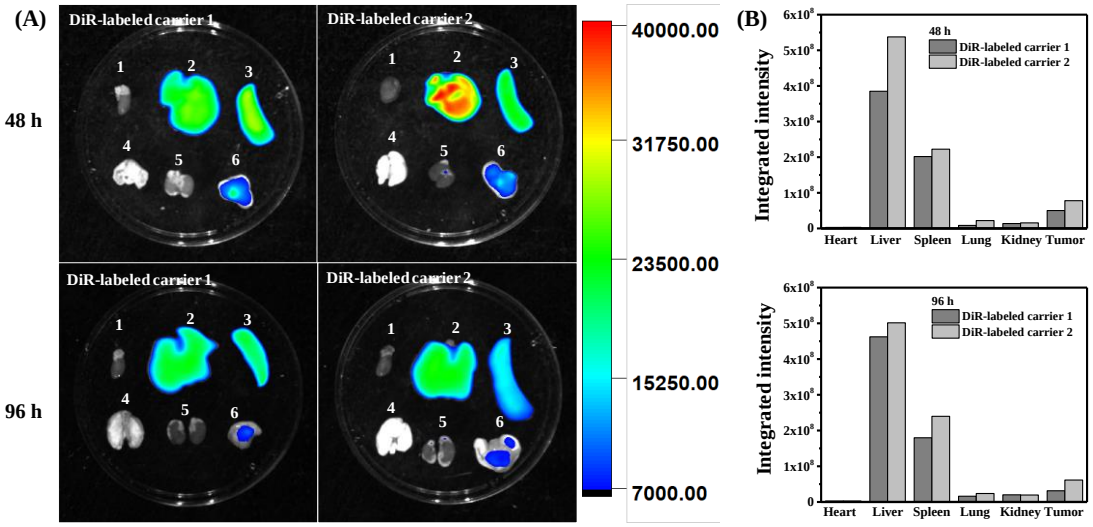

Figure S15. NIR fluorescence of major organs and tumor. (A) NIR fluorescence images of major organs and tumor at 48 and 96 h post-injection. (B) The quantification of fluorescence intensities of major organs and tumor. 1, 2, 3, 4, 5 and 6 represent the heart, liver, spleen, lung, kidney and tumor, respectively. Related to Figure 5.

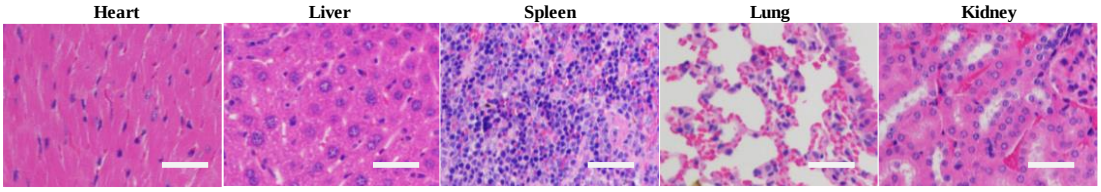

Figure S16. H&E analyse. H&E analyses after the last treatment of Dox-loaded carrier **1**. All scale bars are 100 µm. Related to Figure 5.

2. Transparent Methods

Materials: 2,6-dibromo-4-nitropyridine, 4-bromo-2-methoxyphenylboronic acid, 4-(trimethylsilyl) phenylboronic acid, 4-formylphenylboronic acid, 4-methoxyphenylboronic acid and iodine monochloride (1.0 M solution in dichloromethane) from Aldrich; ethyl L-(-)-lactate, tetrakis (triphenylphosphine) palladium (0) from TCI; 3-chloro-2-chloromethyl-1-propene (96 %) were obtained from Acros and used directly. Sephadex G-50 gel was activated before use. Unless otherwise indicated, all starting materials were obtained from commercial suppliers and were used without purification. Tetrahydrofuran (THF) was dried by distillation from sodium-benzophenone immediately prior to use. Dichloromethane (DCM) was dried by distillation from CaH_2. Distilled water was polished by ion exchange and filtration. Visualization was accomplished with Uv light, iodine vapor. Flash chromatography was carried out with Silica Gel (200-300 mesh). Dulbecco'S Modified Eagle Medium high glucose (DMEM), fetal bovine serum (FBS) and Trypsin-EDTA (0.25%) were from Invitrogen. Hoechst 33258, Paraformaldehyde Fix Solution (4%), Cell Counting Kit-8 were from Beyotime Biotechnology Co., Ltd.; LysoTracker Green DND-26, Calcein-AM/PI Double Stain Kit and 1,1-dioctadecyl-3,3,3,3-tetramethylindotricarbocyanine iodide (DiR) were purchased from Shanghai Yeasen Biotechnology Co., Ltd. Doxorubicin hydrochloride from sigma was deprotonated by adding triethylamine (TEA) prior to use. Matrigel Basement Membrane Matrix was purchased from Corning. Isoflurane was purchased from Shanghai Yuyan Instruments.

General: The purity of the products was checked by thin-layer chromatography (TLC; Merck, silica gel 60). High performance liquid chromatography (HPLC) was performed for further purification by using Hanbon Sci&Tech NP7000 SERIALS PUMP, NU3000 SERIALS Uv-vis DETECOR, C18 column (Hedera ODS-2 column). ^{1}H-NMR and ^{13}C-NMR spectra were recorded from $CDCl_3$ or d_6-DMSO solutions on Bruker AVANCE III 400MHz. All compounds are subjected to ^{1}H NMR analysis to confirm >98% sample purity. Chemical shifts were reported in ppm relative to the residual solvent peak ($CDCl_3$: ^{1}H, 7.29; ^{13}C, 77.35). Multiplicity was indicated as follows: s (singlet), d (doublet), t (triplet), m (multiplet) and dd (doublet of doublets). Coupling constants are reported in Hz. MALDI TOF-MS spectroscopy (MALDI-TOF-MS) was performed on a Bruker ultrafleXtreme using α-cyano-4-hydroxy cinnamic acid (CHCA) as a matrix. The Uv-vis spectra were obtained from a Metash Uv-8000S Spectrophotometer. The fluorescence spectra were obtained from a Shimadzu RF-5301 Fluorescence Spectrophotometer. The transmission electron microscopy (TEM) was performed at 120 kV using JEOL-JEM 2100. The acquisition time for bright field (BF) imaging was 1 s using the smallest objective lens aperture. Annular dark field (ADF)-STEM imaging was also conducted using JEM ARM 200F operated at 80 kV with a probe aberration corrector. Annular dark field (ADF) images were acquired at a 20 mrad convergence angle, collection angle from 50 mrad to 180 mrad and acquisition time 40 μs per pixel. The AFM measurements were performed using Bruker Multimode 8 in air at ambient temperature (ca. 25 °C) on mica with tapping mode. The dynamic light scattering (DLS) and zeta potential experiments were performed by Nano Brook EliteSizer Omni of Brookhaven. The HepG2, HL7702 and 4T1 cell lines were cultured in DMEM supplemented with 10% (v/v) FBS and 1% (v/v) penicillin–streptomycin under the condition of 5% CO_2 and 95% humidity at 37 °C. The cell viability was measured in a Thermo Scientific Varioskan LUX microplate reader by absorbance at 450 nm. The confocal laser scanning microscopy (CLSM) was performed at LSM 710, Carl Zeiss, Göttingen, Germany. The flow cytometry (FCM) was performed at Beckman Coulter Cytomics^{TM} FC 500. Nude mice weighing 20g were purchased from the Model Animal Research Center of Nanjing University. *In vivo* real-time fluorescence imaging was performed with Bruker FX PRO *in vivo* imaging system.

Synthesis of Compound 4: Compound **3** (1.5 g, 1.13 mmol) and 4-bromo-2-methoxyphenylboronic acid (0.57 g, 2.48 mmol) were dissolved in degassed THF (50 mL). Degassed K_2CO_3 aqueous (2 M, 40 mL) was added to the above mixture and then $Pd(PPh_3)_4$ (0.12 g, 0.1 mmol) was added carefully. The mixture was refluxed for 24 hours with vigorous stirring under argon atmosphere. After completion of the reaction as monitored by TLC, the reaction mixture was cooled down to room temperature and extracted with ethyl acetate three times. The combined organic layer was dried over anhydrous $MgSO_4$. The filtrate was condensed under reduced pressure and purified by column chromatography (silica gel) using

ethyl acetate: methanol (15:1 v/v) as eluent to yield 0.87 g (50 %) of yellow liquid. ^{1}H-NMR (400 MHz, $CDCl_3$, δ, ppm): 7.79 (d, *J*=8.0 Hz, 2H), 7.32 (s, 2H), 7.21 (dd, *J*=9.57 Hz, 2H), 7.15 (d, *J*=1.57 Hz, 2H), 4.14 (d, *J*=5.92 Hz, 2H), 3.9 (s, 6H), 3.65-3.32 (m, 88H), 2.45-2.39 (m, 1H), 2.11-2.06 (m, 2H), 1.09 (d, *J*=6.11, 12H).

Synthesis of Compound 5: Compound **4** (0.8 g, 0.52 mmol), and 4'-(trimethylsilyl) biphenyl-4-ylboronic acid (0.31 g, 1.14 mmol) were dissolved in degassed THF (50 mL). Degassed K_2CO_3 aqueous (2 M, 40 mL) was added to the above mixture and then $Pd(PPh_3)_4$ (0.06 g, 0.05 mmol) was added carefully. The mixture was refluxed for 24 hours with vigorous stirring under argon atmosphere. Cooled to room temperature, the layers were separated, and the aqueous layer was then washed twice with methylene chloride. The combined organic layers were dried over anhydrous magnesium sulfate and filtered. The solvent was removed in a rotary evaporator, then dissolved in dichloromethane (300 mL) and a 1.0 M solution of ICl in CH_2Cl_2 (3.64 mL, 3.64 mmol) was added dropwise at -78 ^{o}C. The reaction mixture was stirred for 1 h under nitrogen before 1 M aqueous $Na_2S_2O_3$ (35 mL) solution was added and the solution was stirred for 4 h. The layer was separated, and the aqueous layer was then washed with CH_2Cl_2. The combined organic layer was dried over anhydrous $MgSO_4$. The filtrate was condensed under reduced pressure and purified by column chromatography (silica gel) using ethyl acetate : methanol (15:1 v/v) as eluent to yield 0.86 g (85 %) of yellow liquid. ^{1}H-NMR (400 MHz, $CDCl_3$, δ, ppm): 8.05 (d, *J*=8.0 Hz, 2H), 7.83-7.68 (m, 14H), 7.50-7.35 (m, 8H), 4.37 (d, J=5.92, 2H), 4.13 (s, 6H), 3.68-3.3 (m, 88H), 2.54-2.45 (m, 1H), 2.15-2.06 (m, 2H), 1.09 (d, *J*=6.21, 12H).

Synthesis of Compound 1: Compound **5** (0.4 g, 0.21 mmol), and 4-formylphenylboronic acid (0.068 g, 0.46 mmol) were dissolved in degassed THF (30 mL). Degassed K_2CO_3 aqueous (2 M, 20 mL) was added to the above mixture and then $Pd(PPh_3)_4$ (0.06 g, 0.05 mmol) was added carefully. The mixture was refluxed for 24 hours with vigorous stirring under argon atmosphere. After completion of the reaction as monitored by TLC, the reaction mixture was cooled down to room temperature and extracted with ethyl acetate three times. The combined organic layer was dried over anhydrous $MgSO_4$. The filtrate was condensed under reduced pressure and purified by column chromatography (silica gel) using ethyl acetate: methanol (15:1 v/v) as eluent and then further purified by prep-HPLC to yield 0.24 g (60 %) of white solid. M.P. = 75.1 ℃. ^{1}H-NMR (400 MHz, $CDCl_3$, δ, ppm): 10.09 (s, 2H), 8.09 (d, *J*=8.0 Hz, 2H), 8.0 (d, J=8.0, 4H), 7.86-7.67 (m, 20H), 7.46 (s, 2H), 7.40 (d, J=7.5, 2H), 7.30 (s, 2H), 4.21 (d, *J*=4.52 Hz, 2H), 4.0 (s, 6H), 3.65-3.38 (m, 88H), 2.51-2.44 (m, 1H), 2.14-2.08 (m, 2H), 1.12 (d, *J*=6.11, 12H). ^{13}C-NMR (400 MHz, $CDCl_3$, δ, ppm): 191.90, 157.37, 146.65, 140.90, 138.66, 135.27, 131.95, 130.37, 127.85, 127.70, 127.63, 127.55, 127.46, 119.80, 110.24, 75.00, 74.83, 74.79, 71.93, 70.73, 70.61, 70.58, 70.51, 67.38, 59.03, 55.92, 40.82, 17.12. MALDI-TOF mass: m/z calcd. for $C_{109}H_{145}NO_{27}$ $[M+H]^+$, 1902.35; found: $[M+H]^+$, 1902.56.

Synthesis of Compound 2: Compound **5** (0.4 g, 0.21 mmol), and 4-methoxyphenylboronic acid (0.053 g, 0.46 mmol) were dissolved in degassed THF (30 mL). Degassed K_2CO_3 aqueous (2 M, 20 mL) was added to the above mixture and then $Pd(PPh_3)_4$ (0.06 g, 0.05 mmol) was added carefully. The mixture was refluxed for 24 hours with vigorous stirring under argon atmosphere. After completion of the reaction as monitored by TLC, the reaction mixture was cooled down to room temperature and extracted with ethyl acetate three times. The combined organic layer was dried over anhydrous $MgSO_4$. The filtrate was condensed under reduced pressure and purified by column chromatography (silica gel) using ethyl acetate: methanol (15:1 v/v) as eluent and then further purified by prep-HPLC to yield 0.25 g (64 %) of white solid. M.P. = 81.6 ℃. ^{1}H-NMR (400 MHz, $CDCl_3$, δ, ppm): 8.08 (d, *J*=8.0 Hz, 2H), 7.77-7.68 (m, 16H), 7.63 (d, J=8.56, 4H), 7.45 (s, 2H), 7.40 (dd, *J*=9.46, 2H), 7.30 (d, *J*=1.46, 2H), 7.04 (d, *J*=8.56, 4H), 4.21 (d, *J*=5.4 Hz, 2H), 4.02 (s, 6H), 3.90 (s, 6H), 3.66-3.38 (m, 88H), 2.51-2.44 (m, 1H), 2.14-2.07 (m, 2H), 1.12 (d, *J*=6.11, 12H). ^{13}C-NMR (400 MHz, $CDCl_3$, δ, ppm): 159.35, 157.45, 142.32, 139.98, 138.87, 133.20, 131.91, 128.05, 127.58, 127.35, 127.11, 119.78, 114.31, 110.29, 75.01, 74.83, 71.93, 70.74, 70.58, 70.50, 67.38, 58.99, 55.92, 55.37, 40.85, 17.10. MALDI-TOF mass: m/z calcd. for $C_{109}H_{145}NO_{27}$ $[M+H]^+$, 1906.38; found: $[M+H]^+$, 1906.98.

TEM Experiments: To investigate the structures of **1** and **2** in neutral aqueous solution and acidic aqueous solution with 10 equiv TFA, a drop of the solution (0.02 wt%, respectively) was placed on a graphene-supported film and the solution was allowed to evaporate under ambient conditions. TEM images of carriers with Dox encapsulated were also performed. The dried specimen was observed by using a JEM ARM 200F machine operated at 80 kV to determine aromatic wall within the tubular segments. The wall was further imaged using probe aberration corrector by STEM mode to observe inner diameter. The membranes were transferred onto carbon–coated copper grid and then stained by depositing a drop of uranyl acetate aqueous solution (1 wt%) onto the surface of the loaded grid. After dried, the out-diameter of tubules was detected by JEOL-JEM 2100 at 120 kV.

AFM Experiments: For the AFM measurements of the assembled structures, the aqueous solutions of **1** and **2** (0.02 wt%, respectively) with and without addition of TFA (10 equiv) were prepared and 20 μL of the samples were casted on mica. After slow evaporation under air at room temperature, the AFM experiments were performed with tapping mode. The typical settings of the AFM for the high-magnification observations were as follows: a free amplitude of the oscillation frequency of ca. 1.0-1.5 V, a set-point amplitude of 0.9-1.4 V, and a scan rate of 1.0 Hz.

^{1}H NMR Titration: To verify the external methoxyl ortho to pyridine was responsive to acid, the structural transformation of **2** was confirmed by ^{1}H NMR experiment (400 MHz) upon addition of trifluoroacetic acid (TFA) in $CDCl_3$.

DLS & Zeta Potential Experiments: Dynamic light scattering measurements were performed using He-Ne laser operating at 632.8 nm with 0.02 wt% neutral aqueous solution and CH_3COOH/CH_3COONa buffer solution (pH 4.6), respectively. The scattering was kept at 90^o during the whole experiment at 25 ^{o}C. The hydrodynamic diameter (D_H) was determined from the autocorrelation functions by the time interval method of photon correlation and the CONTIN methods using the software provided by the manufacturer. Size distribution of carriers with Dox encapsulated was also performed. Zeta potential was tested by ZetaPALS methods of NanoBrook EliteSizer Omni of Brookhaven.

The Kinetic Experiment of Dynamic Assembly: To investigate the process of dynamic assembly, the tracing Uv-vis spectra of **2** with different concentrations (0.1, 0.2, 0.3, 0.4, 0.5, 0.6, 0.7, 0.8, 0.9, 1 mg/mL) were performed in different pH value. The 2 nm redshift is observed as a signal of dynamic assembly from tubules to toroids. The changes of maximum absorption wavelength of **2** (0.6 mg/mL) in dynamic assembly from tubules to toroids against time was also performed using the same assay.

Drug Loading and Release Experiments: Drug loading was carried out by sonicating **1** (or **2**) (1 mg) and Dox (0.4 mg) in deionized water (1 mL) at room temperature in the dark for 15 min. The solution of the loaded carriers **1** or **2** was obtained after separating free Dox using sephadex G-50 column and then freeze dried. Since there is no overlap absorbance of carriers and Dox at 485 nm, the loaded Dox and carriers were determined by Uv-vis spectra at 485 nm and 339 nm after dissolved in DMSO. According to determination of loaded drugs and carrier amount, the drug loading efficiency was calculated as 21.4 wt% for **1** and 22.1 wt% for **2**. For the responsive of carriers, the release was performed in mild acidic buffer solution. For the dissolution of loaded carrier **1** or **2** (1 mL) in CH_3COOH/CH_3COONa buffer solution, the released drugs were separated through sephadex G-50 using CH_3COOH/CH_3COONa buffer solution. The separated carriers and drugs also monitored using Uv-vis at 339 nm and 485 nm respectively.

CCK-8 Assay: Proliferation of HepG2, 4T1 and HL7702 cells in the presence of carrier **1** and **2** was determined using a Cell Counting Kit-8 (CCK-8) assay according to the manufacturer's instructions. Briefly, cells were seeded into 96-well culture plates (1×10^4). They were treated with the solutions of the **1** and **2** at different concentrations (0.02, 0.05, 0.1, 0.2, 0.4, 0.6, 0.8, and 1 mg /mL), and PBS as a negative control for 72 h, and cell growth was measured. The *in vitro* cytotoxicity of free Dox, loaded carriers **1** and **2** were also measured using the CCK-8 assay. HepG2, 4T1 or HL7702 cells were seeded into 96-well culture plate with the density of 1×10^4/well. Relative drug concentrations at 0.02, 0.04, 0.08, 0.16, 0.32, 0.64, 1.28, 2.56, or

5.12 μg/mL were added to the treatment group, and PBS as the control group, and the cell proliferation was measured. All the experiments were performed triplicates. The following formula was used to calculate the viability of cell growth:

$$\text{cell viability (\%)} = \frac{A_{treatment}}{A_{control}} \times 100\%$$

where $A_{treatment}$ is the mean of absorbance of each well with background subtraction measured at 450 nm of treatment group; $A_{control}$ is the mean of absorbance of each well with background subtraction measured at 450 nm of control group.

Confocal Laser Scanning Microscopy (CLSM): Intracellular trafficking of Dox in HepG2 cancer cells was examined by confocal microscopy. Cells were seeded into confocal petri dish at 1 × 10^5/well and co-incubated with the loaded carrier **1** or **2** at a Dox dose of 1.28 μg/mL for 2, 6, 12 or 24 h. Cells were further co-incubated with Hoechst 33258 and Lysotracker green DND-26 for 2 h. The cells were thoroughly washed with PBS three times afterwards. Images were obtained using a Carl Zeiss LSM 710 microscope.

Live/Dead Double Staining: The cell killing effects were also investigated by CLSM. HepG2 or HL7702 cells were seeded into 6-well culture plates (1 × 10^6/well) and incubated with the loaded carrier **1** or **2** at a dose of Dox 0.64 μg/mL for 72 h. All Cells were harvested and washed three times with PBS, and then stained with Calcein-AM and PI as manufacturer's protocol at 37 °C for 30 min in the dark. Images were obtained using a Carl Zeiss LSM 710 microscope.

Flow Cytometry (FCM) Assay: The quantitative cellular internalization was investigated by using a flow cytometry (FCM) technique. Cells were seeded into 6-well culture plates (1 × 10^6/well) and co-incubated with the loaded carrier **1** or **2** at a Dox dose of 0.64 μg/mL for 2, 6, 12, 24, 48 or 72h. Cells were washed three times with PBS, and harvested after digestion by Trypsin-EDTA solution (0.25 %), and then washed three times with PBS through centrifugation and resuspended with PBS. Finally, the cells were immediately applied on Beckman Coulter Cytomics™ FC 500, the cells were gated upon acquisition by using forward versus side scatter to exclude debris and dead cells. The data were collected (10,000 cell counts) and analyzed with CXP analysis software. All the experiments were performed triplicates.

Animal Model: Female BALB/c nude mice (4-6 weeks old) were purchased from the Model Animal Research Center of Nanjing University. All experimental procedures for animal studies were performed in accordance with regulation in the Animal Care Committee of Sun Yat-Sen University. To establish the 4T1 tumor model, 1 × 10^6 cells were inoculated subcutaneously into the right front flanks of female BALB/c nude mice. Tumor growth was measured using a caliper, and the tumor volume was calculated using the following formula:

$$\text{volume} = \frac{(tumor\ length) \times (tumor\ width)^2}{2}$$

***In Vivo* Imaging of Carrier:** The tumor-bearing mice models were established as described above. When tumor volume reached a mean size of about 150-200 mm^3, carriers labeled NIR dye DiR were intravenously injected via tail vein at a dose of 1 mg/Kg based on DiR. After administration, *in vivo* real-time fluorescence imaging was performed with Bruker FX PRO *in vivo* imaging system. Scans were carried out at 2, 6, 12, 24, 48, 72 and 96 h post-injection. Additionally, major organs, including heart, liver, spleen, lung, kidney and tumor were collected 48 and 96 h post-injection. Fluorescent images of the collected tissues were captured using Bruker FX PRO *in vivo* imaging system.

***In Vivo* Antitumor Efficacy:** The tumor-bearing mice models were established as described above. When tumor volume reached a mean size of about 150-200 mm^3, the mice were randomly divided into four groups (n = 4 in each group). The four groups were treated with different indicated reagents as following: Group 1 (negative control) was only injected with saline via tail vein; Group 2 was injected with free Dox; Group 3 was injected with Dox-loaded carrier of **1**; Group 4 was injected with Dox-loaded carrier of **2**. The dose of Dox of Group 2, 3 and 4 were at 3 mg/Kg. Two days after another treatment, tumor sizes and the body weights were also measured for 14 days every two days.

Histopathological Examinations: After the last treatment, animals were sacrificed to obtain the major organs including heart, liver, spleen, lung and kidney. The organs were excised and fixed with 10 % neutral buffered formalin and embedded in paraffin, slices were stained with hematoxylin-eosin (H&E) to evaluate for leukocyte infiltration, cell death, and other signs of organ damage.

Statistical Analysis: All quantitative data are presented as mean±standard deviation. Statistical analyses were performed with the Student's t-test. Differences were considered statistically significant at $p<0.05$ (*).